Orientation Distribution Within a Single Hematite Crystal

**Ralf Hielscher · Helmut Schaeben ·
Heinrich Siemes**

Abstract While crystallography conventionally presumes that a single crystal carries a unique crystallographic orientation, modern experimental techniques reveal that a single crystal may exhibit an orientation distribution. However, this distribution is largely concentrated; it is extremely concentrated when compared with orientation distributions of polycrystalline specimen. A case study of a deformation experiment with a single hematite crystal is presented, where the experimental deformation induced twining, which in turn changed a largely concentrated unimodal "parent" orientation distribution into a multimodal orientation distribution with a major mode resembling the parent mode and three minor modes corresponding to the progressive twining. The free and open source software MTEX for texture analysis was used to compute and visualize orientations density functions from both integral orientation measurements, i.e. neutron diffraction pole intensity data, and individual orientation measurements, i.e. electron back scatter diffraction data. Thus it is exemplified that MTEX is capable of analysing orientation data from largely concentrated orientation distributions.

R. Hielscher
Applied Functional Analysis, TU, 09126 Chemnitz, Germany

H. Schaeben (✉)
Geoscience Mathematics and Informatics, TU Bergakademie, 09596 Freiberg, Germany
e-mail: helmut.schaeben@geo.tu-freiberg.de

H. Siemes
RWTH, 52056 Aachen, Germany

1 Introduction

While crystallography conventionally presumes that a single crystal carries a unique crystallographic orientation, modern experimental techniques reveal that a single crystal may exhibit an orientation distribution. Here a single hematite crystal is experimentally deformed by 3.4% in compression perpendicular to $c(0001)$ at $600°$ Celsius, a strain rate of 10^{-5}/s, and 300 MPa confining pressure. Then its texture is measured by neutron diffraction and by electron back scatter diffraction (Siemes et al. 2008). To analyse and visualize these measurements we use the free and open source Matlab® software toolbox MTEX for texture analysis (Hielscher 2007; Hielscher and Schaeben 2008a, 2008b; Schaeben et al. 2007). A unique feature of the MTEX toolbox is that it provides a unifying approach to texture analysis with integral ("pole figure") or individual ("EBSD") orientation measurements. Therefore, it is particularly well suited to compare patterns of preferred orientation based on data of such different origin. Moreover, it is exemplified that the mathematical method and its numerical realisation encoded in the MTEX toolbox applies to high resolution pole figure data and sharp textures, and that computations of harmonic coefficients, modal orientations, volume portions, texture index, entropy, etc. are possible for both kind of data. Comparing the results based on neutron diffraction or electron back scatter diffraction, it is concluded that they agree very well and support a plausible interpretation.

2 Preliminaries: Crystallographic Orientation, Orientation Density Function, Pole Density Function

We commence with the definition of the orientation of a crystal within a polycrystalline specimen. Let $\mathcal{K}_S = \{\mathbf{x}, \mathbf{y}, \mathbf{z}\}$ be a right-handed orthogonal specimen coordinate system, and let $\mathcal{K}_C = \{\mathbf{a}, \mathbf{b}, \mathbf{c}\}$ be a right-handed orthogonal crystal coordinate system. Then we call a rotation $g \in \mathrm{SO}(3)$ orientation of the crystal if it rotates the specimen coordinate system onto the crystal coordinate system, i.e. $g\mathbf{x} = \mathbf{a}$, $g\mathbf{y} = \mathbf{b}$, $g\mathbf{z} = \mathbf{c}$. Let $\mathbf{r} = (u, v, w)^\mathsf{T}$ be a coordinate vector with respect to the specimen coordinate systems $\mathcal{K}_S$, and let $\mathbf{h} = (h, k, l)^\mathsf{T}$ be the corresponding coordinate vector with respect to the crystal coordinate system $\mathcal{K}_C$, i.e. both coordinate vectors represent the same direction, and we have

$$u\mathbf{x} + v\mathbf{y} + w\mathbf{z} = h\mathbf{a} + k\mathbf{b} + l\mathbf{c}.$$

Then, the orientation $g \in \mathrm{SO}(3)$ identified with a matrix in $\mathbb{R}^{3 \times 3}$ realizes the basis transformation between the coordinate systems, and we have the equation

$$g\mathbf{h} = \mathbf{r}.$$

Since the crystal coordinate system can be assigned to the crystal uniquely only up to crystal symmetry, every orientation $g \in \mathrm{SO}(3)$ is associated with a whole class of crystallographically equivalent orientations. Crystallographic symmetries are commonly described by symmetry groups. When analysing diffraction data for preferred crystallographic orientation, it is sufficient to consider the restriction of the Laue

group $G_{\text{Laue}} \subset \text{O}(3)$ to its purely rotational part $\widetilde{G}_{\text{Laue}} = G_{\text{Laue}} \cap \text{SO}(3)$. Then two orientations $g, g' \in \text{SO}(3)$ are called crystallographically symmetrically equivalent with respect to $\widetilde{G}_{\text{Laue}}$ if there is a symmetry element $q \in \widetilde{G}_{\text{Laue}}$ such that $gq = g'$. The left cosets $g\widetilde{G}_{\text{Laue}}$ define the classes of crystallographically symmetrically equivalent orientations. They define a partition of SO(3). A set of class representatives, which contains exactly one element of each left coset or class, is called a left transversal. It is not unique. If it is easily tractable with respect to a parametrization, it will be denoted $\mathbb{G}$. Then $\mathbb{G}$ is a subset of SO(3) which contains each physically distinct orientation exactly once. Many different names have been used for this region, e.g. asymmetric domain (or unit or region), symmetrically equivalent area, fundamental zone, MacKenzie cell (cf. Morawiec 1997). Analogously, two crystallographic directions $\mathbf{h}, \mathbf{h}' \in \mathbb{S}^2$ are called crystallographically equivalent if there is a symmetry element $q \in \widetilde{G}_{\text{Laue}}$ such that $q\mathbf{h} = \mathbf{h}'$.

The orientation density function (ODF) of a specimen is defined as the probability density function

$$f : \text{SO}(3) \to \mathbb{R}$$

which models the relative frequencies of crystal orientations within the specimen by volume (Bunge 1969; Bunge and Morris 1982). The ODF possesses the symmetry property

$$f(g) = f(gq), \quad g \in \text{SO}(3), \ q \in \widetilde{G}_{\text{Laue}} \tag{1}$$

and is normalized to

$$\int_{\text{SO}(3)} f(g)\,\mathrm{d}g = 8\pi^2, \tag{2}$$

where $\mathrm{d}g$ denotes the rotational invariant measure on SO(3). Given $\widetilde{G}_{\text{Laue}}$, the domain of definition of f can for all practical purposes be restricted to the corresponding $\mathbb{G}$.

The texture index of an orientation density function f is defined as

$$I(f) = \int_{\text{SO}(3)} f(g)^2\,\mathrm{d}g, \tag{3}$$

the entropy of an orientation density function f is defined as

$$S(f) = -\int_{\text{SO}(3)} f(g)\ln f(g)\,\mathrm{d}g. \tag{4}$$

Both provide a measure of the degree of preferred orientation, i.e. a measure of deviation from the uniform distribution.

The axis distribution function (Bunge 1969; Bunge and Morris 1982) or pole density function (PDF) (Matthies et al. 1987) of a specimen is defined as the function

$$P : \mathbb{S}^2 \times \mathbb{S}^2 \to \mathbb{R}$$

which models the relative frequencies of specific lattice plane orientations, i.e. the relative frequencies of normal vectors of specified lattice planes, within the specimen

by volume. Mathematically the PDF P corresponding to an ODF f is characterized by the fundamental equation of texture analysis (Bunge 1969; Bunge and Morris 1982)

$$P(\mathbf{h}, \mathbf{r}) = \frac{1}{2}\big(\mathcal{R}f(\mathbf{h}, \mathbf{r}) + \mathcal{R}f(-\mathbf{h}, \mathbf{r})\big),$$

$$\mathcal{R}f(\mathbf{h}, \mathbf{r}) = \frac{1}{2\pi} \int_{G(\mathbf{h}, \mathbf{r})} f(g)\, \mathrm{d}g, \tag{5}$$

where the path of integration $G(\mathbf{h}, \mathbf{r}) := \{g \in \mathrm{SO}(3) \mid g\mathbf{h} = \mathbf{r}\}$ is defined as the set ("fibre") of all rotations which map the crystallographic direction $\mathbf{h} \in \mathbb{S}^2$ onto the specimen direction $\mathbf{r} \in \mathbb{S}^2$. The fundamental equation of texture analysis involves the integral operator $\mathcal{R}$, recently recognized as the totally geodesic Radon transform (Schaeben and Boogaart 2003). The properties (1) and (2) of an ODF f imply the following properties of the corresponding PDF P,

$$P(\mathbf{h}, \mathbf{r}) = P(q\mathbf{h}, \mathbf{r}), \quad \mathbf{h}, \mathbf{r} \in \mathbb{S}^2, \ q \in \widetilde{G}_{\mathrm{Laue}},$$

and

$$\int_{\mathbb{S}^2} P(\mathbf{h}, \mathbf{r})\, \mathrm{d}\mathbf{h} = \int_{\mathbb{S}^2} P(\mathbf{h}, \mathbf{r})\, \mathrm{d}\mathbf{r} = 4\pi.$$

Eventually, we are interested in superpositions

$$\sum_{\mathbf{h} \in H_i} \rho_{\mathbf{h}} \mathcal{R}f(\mathbf{h}, \mathbf{r}) = \mathcal{R}f(H_i, \boldsymbol{r})$$

where $H_i = H(\lambda_i, \theta_i)$ is a set of superimposing crystal directions depending on a wavelengths λ_i and Bragg angles θ_i, and $\rho_{\mathbf{h}}, \mathbf{h} \in H_i$, are the relative reflection intensities.

Then the experimental pole intensity data are modelled as

$$\mathbf{I}_{ij_i} \sim a_i \sum_{\mathbf{h} \in H_i} \rho_{\mathbf{h}} \mathcal{R}f(\mathbf{h}, \mathbf{r}_{ij_i}) + I_{ij_i}^b = a_i \mathcal{R}f(H_i, \boldsymbol{r}_{j_i}) + I_{ij_i}^b$$

where $i = 1, \ldots, N$ is the number of pole figures, $j_i = 1, \ldots, N_i$ is the number of specimen directions, $H_i = H(\lambda_i, \theta_i)$ is the superposed crystal directions, $\rho_{\mathbf{h}}, \mathbf{h} \in H_i$ is the relative reflection intensities, $\mathbf{r}_{ij_i}$ is the specimen directions, $\mathbf{I}_{ij_i}$ is the diffraction counts, $I_{ij_i}^b$ is the background intensities, $f\colon \mathrm{SO}(3) \to \mathbb{R}_+$ is an ODF, $a_i \in \mathbb{R}_+$ is the normalization constants.

In practice, the problem is to construct a reasonable approximation of the orientation probability density function f explaining the experimental intensities in the "least-squares" sense

$$\sum_{i=1}^{N} \sum_{j_i=1}^{N_i} \big(a_i \mathcal{R}f(H_i, \boldsymbol{r}_{j_i}) + I_{ij_i}^b - \boldsymbol{I}_{ij_i}\big)^2 \to \min,$$

where $a_i, i = 1, \ldots, N$, are generally unknown. For more details, the reader is referred to Hielscher and Schaeben (2008a, 2008b).

3 Radially Symmetric Functions in Texture Analysis

In texture analysis, radially symmetric functions appear as unimodal bell-shaped "standard" or model ODFs. Mathematically they are defined as functions $\psi: \text{SO}(3) \to \mathbb{R}$ which do not depend on the rotation g but only on the angle $\omega(g)$ of rotation, i.e. given a center rotation $g_0 \in \text{SO}(3)$, we have

$$\psi(g; g_0) = \psi(g'; g_0)$$

for all rotations $g, g' \in \text{SO}(3)$ with $\omega(gg_0^{-1}) = \omega(g'g_0^{-1})$. Analogously to the spherical case (cf. Dunkl 1966), there is an isomorphism between radially symmetric functions ψ defined on SO(3) and associated functions Ψ defined on $[-1, 1]$ (Hielscher 2007). It is well known that all pole figures of radially symmetric ODFs are radially symmetric.

Let κ be a parameter within a set $\mathbb{A}$, which is either an interval (a, b) with $0 \le a < b \le \infty$ or $\mathbb{N}$, and let κ_0 be either a, b, or ∞. The family of radially symmetric functions $(\psi_\kappa(\omega(g)), \kappa \in \mathbb{A})$ on SO(3) centered at the identity of SO(3) with a parameter $\kappa \in \mathbb{A}$ controlling the localization is called a kernel if

$$\frac{1}{8\pi^2} \int_{\text{SO}(3)} \psi_\kappa\big(\omega(g)\big)\, dg = 1 \quad \text{for all } \kappa \in \mathbb{A}. \tag{6}$$

If $\psi_\kappa \ge 0, \kappa \in \mathbb{A}$, then (6) implies in particular the uniform boundedness of $(\psi_\kappa, \kappa \in \mathbb{A})$ with respect to its L^1-norm. In practice, ψ_κ are often non-negative unimodal bell-shaped functions with their parameter $\kappa \in \mathbb{A}$ controlling the width of the graph of ψ_κ.

Example 1 An example of a well localized, non-negative, radially symmetric function on SO(3) is the de la Vallée Poussin kernel (Schaeben 1997, 1999; Hielscher 2007). It is given for any $\kappa \in \mathbb{N}$ by

$$\psi(g; g_0) = \frac{B(\frac{3}{2}, \frac{1}{2})}{B(\frac{3}{2}, \kappa + \frac{1}{2})} \cos^{2\kappa} \frac{\omega(gg_0^{-1})}{2}.$$

Its Radon transform reads

$$\mathcal{R}\psi(\mathbf{h}, \mathbf{r}) = \frac{1 + \kappa}{2^\kappa}(1 + g_0\mathbf{h} \cdot \mathbf{r})^\kappa = (1 + \kappa)\cos^{2\kappa}\big(\arccos(g_0\mathbf{h} \cdot \mathbf{r})\big).$$

The parameter κ controls the halfwidth of the kernel. For illustration of the de la Vallée Poussin kernel ψ, its Radon transform $\mathcal{R}\psi$ and its Chebyshev coefficients $\widehat{\psi}$ are plotted in Fig. 1. It is emphasized that the harmonic series expansion of the de la Vallée Poussin kernel is finite. For $\kappa \in \mathbb{N}$ it is obvious, as the de la Vallée Poussin kernel is just a well normalized even power of cosine.

A kernel $(\psi_\kappa, \kappa \in \mathbb{A})$ is an approximate identity if (Freeden et al. 1998)

$$\lim_{\kappa \to \kappa_0} \int_{\omega(gg_0^{-1}) \ge \delta} \psi_\kappa\big(\omega(gg_0^{-1})\big)\, dg = 0, \tag{7}$$
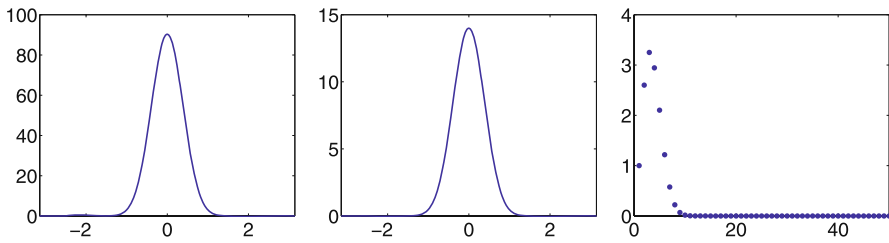
Fig. 1 The de la Vallée Poussin kernel ψ_κ for $\kappa = 7$, its Radon transform $\mathcal{R}\psi_\kappa$, and its Chebyshev coefficients $\widehat{\Psi}$

or

$$\lim_{\kappa \to \kappa_0} \left[\sup_{\omega(gg_0^{-1}) \geq \delta} \psi_\kappa\big(\omega(gg_0^{-1})\big) \right] = 0. \tag{8}$$

Thus, as $\kappa \to \kappa_0$, the kernel ψ_κ approximates Dirac's δ-function. In order to consider crystal symmetry, we define symmetrized radially symmetric functions

$$\psi_{\widetilde{G}_{\text{Laue}}}(g) = \frac{1}{|\widetilde{G}_{\text{Laue}}|} \sum_{q' \in \widetilde{G}_{\text{Laue}}} \psi(gq') = \psi(g\widetilde{G}_{\text{Laue}})$$

which are effectively defined on $\mathbb{G} \subset SO(3)$.

4 Orientation Density Estimation with Integral Orientation Measurements

Let $g_1, \ldots, g_M \in SO(3)$ be an approximate equidistribution in $SO(3)$ with resolution $\delta = \min_{m \neq m'} \omega(g_m g_{m'}^{-1})$. Then, we apply the model assumption that there are coefficients $\boldsymbol{c} \in \mathbb{R}_+^M$ such that

$$f(g) \sim \sum_{m=1}^{M} c_m \psi_\kappa\big(\omega(gg_m^{-1})\big).$$

Since the Radon transform is linear, its application to the superposition of radially symmetric functions results in

$$\mathcal{R}f(\boldsymbol{h}, \boldsymbol{r}) = \sum_{m=1}^{M} c_m \mathcal{R}\psi_\kappa(g_m \boldsymbol{h} \cdot \boldsymbol{r}).$$

Then, the finite dimensional minimization problem to be solved for the unknown normalization constants $a_i \in \mathbb{R}_+$ and the unknown weights $c_m \in \mathbb{R}_+$ is

$$J(\mathbf{c}, \mathbf{a}) = \sum_{i=1}^{N} \sum_{j=1}^{N_i} \frac{(a_i \sum_{m=1}^{M} c_m \mathcal{R}\psi_\kappa(g_m H_i, \boldsymbol{r}_{ij_i}) + I_{ij_i}^b - \boldsymbol{I}_{ij_i})^2}{\boldsymbol{I}_{ij_i}} \to \min$$

subject to constraints $\mathbf{a} \geq 0, \mathbf{c} \geq 0, \sum_{m=1}^{M} c_m = 1$, and setting $H_i = H(\lambda_i, \theta_i)$ is the superposed crystal directions, $\mathbf{r}_{ij_i}$ is the specimen directions, $\mathbf{I}_{ij_i}$ is the diffraction counts, $I_{ij_i}^b$ is the background intensities, $\psi_\kappa : \mathrm{SO}(3) \to \mathbb{R}$ is the radially symmetric functions, $g_m \in \mathrm{SO}(3)$ is the approx. uniform grid of rotations, $m = 1, \ldots, M$.

Estimation of the normalization constants can explicitly be rewritten as

$$a_i(f) = \frac{\sum_{j_i=1}^{N_i} \mathbf{I}_{ij_i} - I_{ij_i}^b}{\sum_{j=1}^{N_i} \mathcal{R} f(H_i, \mathbf{r}_{ij_i})}.$$

Summarly, the recipe of the novel method comprises

1. Choosing a radial basis function $\psi : \mathrm{SO}(3) \to \mathbb{R}$
2. Choosing an approximate equidistribution of orientations $g_1, \ldots, g_M \in \mathrm{SO}(3)$
3. Representing the unknown ODF as a superposition of unimodal ODFs $f(g) = \sum_{m=1}^{M} c_m \psi_\kappa(g g_m^{-1})$
4. Computing the coefficients $c_1, \ldots, c_m$ by minimizing the functional J.

For more details, the reader is referred to Hielscher and Schaeben (2008a, 2008b). A measure of goodness-of-fit is provided by

$$\mathrm{RP}(H_i) = \sum_{j=1}^{N_i} \frac{(a_i \sum_{m=1}^{M} c_m \mathcal{R} \psi_\kappa(g_m H_i, \mathbf{r}_{ij_i}) + I_{ij_i}^b - \mathbf{I}_{ij_i})^2}{\mathbf{I}_{ij_i}}.$$

5 Non-parametric Kernel Density Estimation with Individual Orientation Data

Non-parametric kernel density estimation on SO(3) is applied analogously to spherical density estimation (Schaeben 1982; Parzen 1962; Tapia and Thompson 1978; Hall et al. 1987). It may be seen as a convolution of a kernel chosen by the user and the discrete uniform measure assigning to each observation the probability $\frac{1}{n}$, where n denotes the sample size. Any kernel density estimation inevitably involves some smoothing, the extent of the smoothing depending on the "width" of the kernel controlled by its parameter κ, or its bandwidth, respectively. In fact, choosing the proper kernel width is critical, much more critical than the choice of the kernel itself (cf. Scott 1992, p. 133).

Let $g_i \in \mathrm{SO}(3), i = 1, \ldots, n$, be a sample of individual orientation measurements of sample size n. Should the measurements initially be spatially referenced, this reference is neglected here. In fact, the sample is seen as a realization of a mathematical sample of random orientations $G_i : (\theta, \mathcal{A}, P) \to (\mathrm{SO}(3), \mathcal{B}(\mathrm{SO}(3))), i = 1, \ldots, n$, which are assumed to be identical independent distributed with finite expectation and finite variance. Then, the basic kernel density estimator is defined as

$$f_\kappa^*(g; G_1, \ldots, G_n) = \frac{1}{n} \sum_{i=1}^{n} \psi_\kappa\big(\omega\big(g G_i^{-1}\big)\big), \quad \kappa \in \mathbb{A},$$

where $(\psi_\kappa, \kappa \in \mathbb{A})$ is actually an approximate identity. It should be noted that the estimator is a random variable itself. An actual estimate is given by

$$f_\kappa^*(g; g_1, \ldots, g_n) = \frac{1}{n} \sum_{i=1}^n \psi_\kappa\big(\omega\big(gg_i^{-1}\big)\big), \quad \kappa \in \mathbb{A}.$$

Since it will be clear by the context if the random estimator or its corresponding estimate is meant, they are not distinguished, but both denoted f_κ^*. Formally, the actual estimate differs from the estimator by replacing G_i by their realizations g_i, $i = 1, \ldots, n$.

Considering crystal symmetry, the basic kernel density estimator is generalized to

$$f_\kappa^*\big(g; G_1\widetilde{G}_{\text{Laue}}, \ldots, G_n\widetilde{G}_{\text{Laue}}\big) = \frac{1}{n} \sum_{i=1}^n \frac{1}{\#\widetilde{G}_{\text{Laue}}} \sum_{\sigma \in \widetilde{G}_{\text{Laue}}} \psi_\kappa\big(\omega\big(gG_i^{-1}\sigma\big)\big)$$

$$= \frac{1}{n} \sum_{i=1}^n \psi_\kappa\big(\omega\big(gG_i^{-1}\widetilde{G}_{\text{Laue}}\big)\big), \quad \kappa \in \mathbb{A},$$

and is thought of as being effectively defined on $\mathbb{G} \subset \text{SO}(3)$. As usually, the Radon transform of $f_\kappa^*(g; G_1\widetilde{G}_{\text{Laue}}, \ldots, G_n\widetilde{G}_{\text{Laue}})$ is given by

$$\mathcal{R}\big[f_\kappa^*\big(\circ; G_1\widetilde{G}_{\text{Laue}}, \ldots, G_n\widetilde{G}_{\text{Laue}}\big)\big](\boldsymbol{h}, \boldsymbol{r}) = \frac{1}{n} \sum_{i=1}^n \mathcal{R}\psi_\kappa\big(G_i\widetilde{G}_{\text{Laue}}\boldsymbol{h} \cdot \boldsymbol{r}\big)$$

$$= \frac{1}{n} \sum_{i=1}^n \mathcal{R}\psi_\kappa(G_i\boldsymbol{h} \cdot \boldsymbol{r}),$$

and is itself again a random variable. The mathematical properties of the kernel density estimator will be pursued by the authors elsewhere.

6 Practical Example of a Hematite Texture

Using MTEX we shall elaborate on the methodological aspects of analysis of preferred crystallographic orientation of a hematite specimen H43C1 which has been interpreted in terms of experimental deformation by Siemes et al. (2008). The twofold subject of their communication are the evaluation of the glide modes of hematite and their critical resolved shear stresses depending on deformation temperature.

Hematite, Fe_2O_3, is a trigonal mineral with corundum structure and a hexagonal cell with $a_0 = 0.5038$ nm, $c_0 = 1.3772$ nm, to which the symbols for planes $(hkil)$, sets of symmetry related planes $\{hkil\}$, directions $[uvtw]$, and sets of symmetry related directions $\langle uvtw \rangle$ refer. Tetragonal prismatic specimen sized $7 \times 7 \times 14$ mm^3 were prepared from naturally grown single crystals in different crystallographic orientations with their top plane either parallel to $c(0001)$, $r(01\bar{1}2)$, $f(10\bar{1}1)$, $a(11\bar{2}0)$,

Fig. 2 Stress–strain curve of specimen H43C1 deformed by 3.4% in compression perpendicular to $c(0001)$
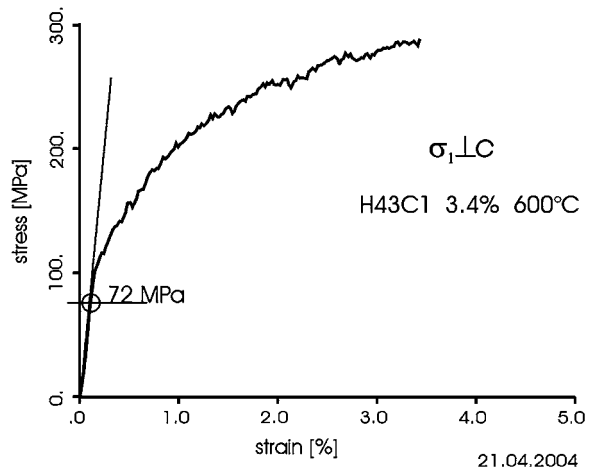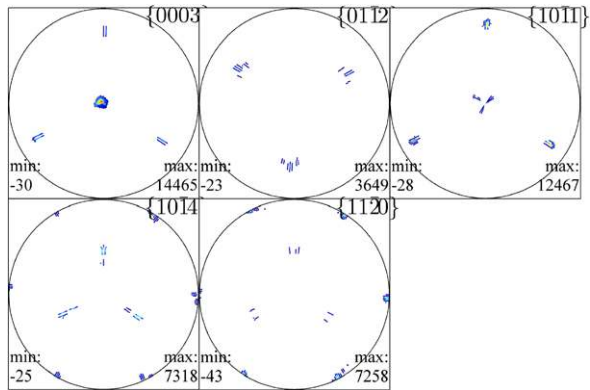

Fig. 3 Experimental pole figures (equal area projection, upper hemisphere) of the reflections $c(0001)$, $f(10\bar{1}1)$, $r(01\bar{1}2)$, $e(10\bar{1}4)$, and $a(11\bar{2}0)$ measured by neutron diffraction with specimen H43C1 deformed by 3.4% in compression perpendicular to $c(0001)$


or $m(10\bar{1}0)$, respectively. These specimens with different crystallographic orientations are necessary in order to initiate different glide modes, as translation glide (slip) and twin gliding.

Compression tests were performed at the Geoforschungszentrum Potsdam using a high temperature high pressure gas-medium apparatus (Paterson 1970, 1990). Figure 2 shows a stress–strain curve of specimen H43C1 deformed by 3.4% in compression perpendicular to $c(0001)$ at 600° Celsius, a strain rate of 10^{-5}/s, and 300 MPa confining pressure. Indicated is the onset of deviation from linear increase of the stress strain curve. For details concerning the equipment and the experimental procedure, see Siemes et al. (2008).

6.1 Integral Orientation Measurements with Neutron Diffraction

Complete pole figures (Fig. 3) representing the crystallographic preferred orientations of the bulk volume of specimen H43C1 were measured with a neutron texture-diffractometer SV7 (Jansen et al. 2000) at the Research Center Juelich. Since this diffractometer is equipped with a position sensitive detector, the reflections of $c(0003)$,

Fig. 4 Application of zero-range method, white areas indicating zero-intensity areas
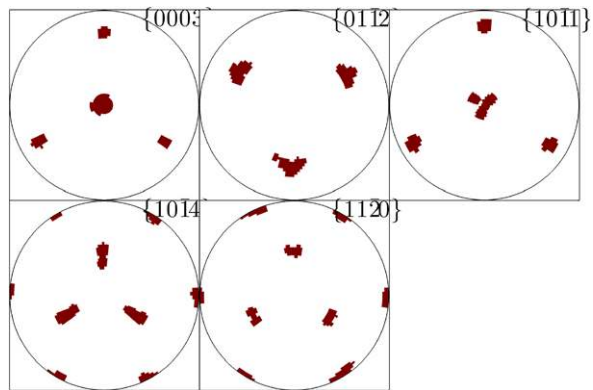
$r\{01\bar{1}2\}$, $f\{10\bar{1}1\}$, $e\{10\bar{1}4\}$, and $a\{11\bar{2}0\}$ were simultaneously measured for a 2Θ-range of 50 degrees using a wavelength of 0.2332 nm, with $c(0001)$ obtained from the third order reflection (0003). To detect the very sharp peaks of the single crystals the standard scanning grid comprising about 500 sample positions was extended to 14616 positions with a mean distance of $1.5°$ which require a measuring time of about three days. The corrected intensity data were plotted in an equal area projection oriented parallel to the (0001) top plane of the specimen.

The neutron diffraction pole figures (Fig. 3) of the bulk volume of specimen H43C1 show the major parent position and three weaker twin positions. In compression tests perpendicular to $c(0001)$, the three r-planes are in an orientation of high shear stress to activate r-twinning. Here the zero-range approximation was applied to speed up the computation of an ODF. This approximation is particularly useful for sharp textures with large areas of zero intensity in the experimental pole figures (Fig. 4). In this case, the ODF is initialized to be zero for all orientations which correspond to a zero-intensity direction in the experimental pole figures. In this way, the computational time is greatly reduced and the resolution of the ODF may be largely improved.

Then, instead of a total of 743,120 only a total of 533 de la Vallée Poussin kernels with a halfwidth of 1.5 degree corresponding to a bandwidth of 286 were fitted to explain the data. The time elapsed to compute the ODF was 271 seconds with a notebook equipped with a Core 2 Duo CPU with 1.86 GH cpu-frequency and 2 GB RAM. The computed orientation density is displayed in 12 σ-sections of Fig. 5. Its texture index is approximately 3400, the entropy is approximately -7.35. There is a major mode at $(155, 3, 53)$ computed by MTEX in terms of an Euler angle triplet using Matthies' **y**-convention. The corresponding volume portion in the 10 degree neighbourhood of the major mode is approximately 0.45, the value of the ODF at the major mode is approximately 14.709. Three minor modes are recognized by visual inspection at about $(90, 65, 59)$, $(30, 115, 1)$, and $(150, 115, 1)$, respectively. The three minor modes are related to one another by rotations of 120 degrees about the specimen z-axis. The corresponding volume portions in the 10 degree neighbourhood of the three minor modes are approximately 0.09, 0.18, and 0.09, respectively; they sum to approximately 0.36. The values of the ODF at the three minor modes are
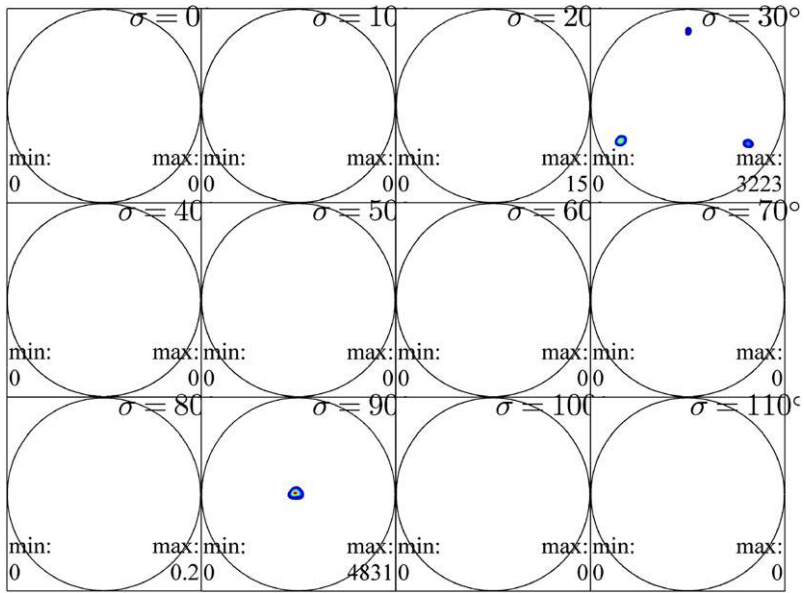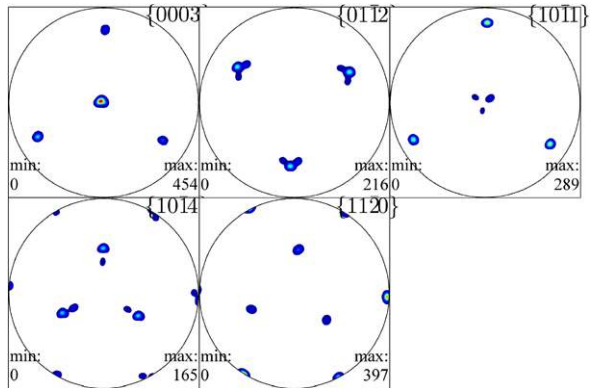
Fig. 5 σ-sections of MTEX's recovered ODF based on experimental pole figures of the reflections $c(0001)$, $r(01\bar{1}2)$, $f(10\bar{1}1)$, $e(10\bar{1}4)$, and $a(11\bar{2}0)$

Fig. 6 Recalculated pole figures (equal area projection, upper hemisphere) of the reflections $c(0001)$, $r(01\bar{1}2)$, $f(10\bar{1}1)$, $e(10\bar{1}4)$, and $a(11\bar{2}0)$

1, 675, 715, and 573. The recalculated pole figures are displayed in Fig. 6, the relative ℓ^1-norm errors (RP errors) are RP$(0001) = 0.55$, RP$(01\bar{1}2) = 0.75$, RP$(10\bar{1}1) = 0.87$, RP$(10\bar{1}4) = 0.70$, RP$(11\bar{2}0) = 0.90$ for the five crystal forms $c(0001)$, $r(01\bar{1}2)$, $f(10\bar{1}1)$, $e(10\bar{1}4)$, and $a(11\bar{2}0)$ considered. Then, the plots of the experimental pole figures are augmented with the pole points corresponding to the major and minor modes and shown in Fig. 7, where the major mode depicted black represents the parent crystal orientation, and the three minor modes depicted blue, red, and green, respectively, indicate three r-twin orientations. The texture based on integral neutron diffraction data may be characterized by some numbers as follows. Computations
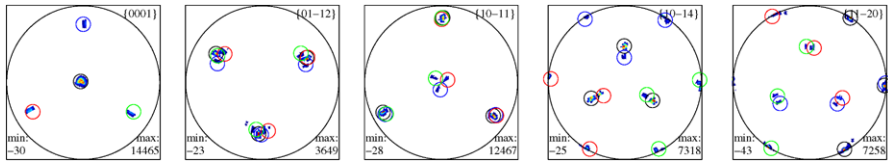
Fig. 7 Experimental pole figures (equal area projection, upper hemisphere) of the reflections $c(0001)$, $r(01\bar{1}2)$, $f(10\bar{1}1)$, $e(10\bar{1}4)$, and $a(11\bar{2}0)$ augmented with major mode $(155, 3, 53)$ (*black*), and minor modes $(90, 65, 59)$ (*blue*), $(30, 115, 1)$ (*red*), and $(150, 115, 1)$ (*green*), respectively

Table 1 The major mode g_M and the three minor modes g_{m_i}, $i = 1, 2, 3$, are given in terms of Euler angles (α, β, γ) (zyz-convention) (left column), and characterized by their probability mass according to the orientation density function in a ball $b(g_m; 10)$ of 10 degrees (center column), and their values of the orientation density function $f(g_m)$

Neutron	(α, β, γ)	$\int_{b(g_m;10)} f(g)\,dg$	$f(\alpha, \beta, \gamma)$
g_M (black)	$(155, 3, 53)$	0.45	14,709
g_{m_1} (blue)	$(90, 65, 59)$	0.09	1,675
g_{m_2} (red)	$(30, 115, 1)$	0.18	715
g_{m_3} (green)	$(150, 115, 1)$	0.09	573
Sum		0.36	

Fig. 8 Specimen H43C1 deformed 3.4% in compression perpendicular to $c(0001)$. OIM® maps of both side planes of the specimen with three r-twins (*blue*, *red*, and *green*)
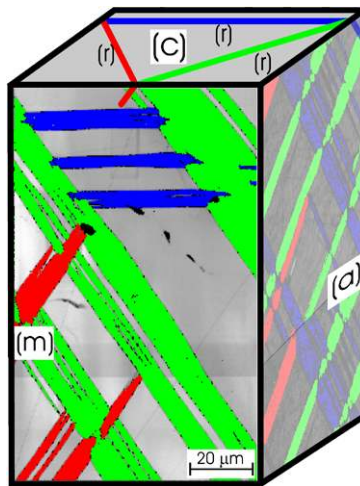
yielded a texture index $J = 3400$, and an entropy $E = -7.35$. Analysis of major and minor modes is summarized in Table 1.

6.2 Individual Orientation Measurements with Electron Back Scatter Diffraction

Electron back scatter diffraction (EBSD) measurements (Kunze et al. 1993) were performed on a SEM CamScan CS44LB equipped with an EBSD attachment at ETH
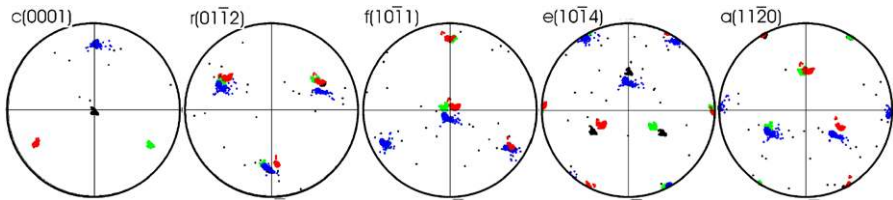
Fig. 9 Specimen H43C1 deformed 3.4% in compression. Pole point figures (equal area projection, upper hemisphere) of plane (*m*) rotated in a position with the compression direction perpendicular to the plane of projection: parent crystal (*black*), three *r*-twins (*blue*, *red*, and *green*). The colours in the pole figures correspond to those in the OIM$^{\text{Ù}}$ maps of Fig. 8
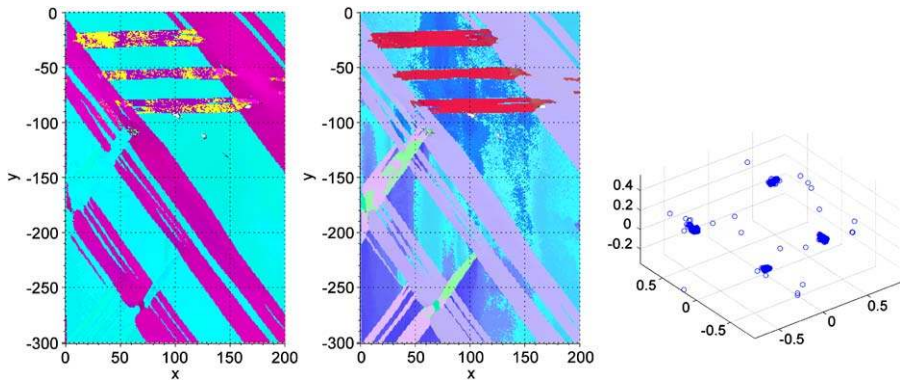

Fig. 10 RGB- and IHS-colour coded raw EBSD measurements of specimen H43C1 deformed by 3.4% in compression perpendicular to *c*(0001) (*left* and *center*), EBSD measurements in Rodrigues space (*right*)

Zurich, Switzerland, and a total of 69,541 individual orientations were measured. Using the processing software OIM® (EDAX–TSL Inc.), orientation image microscopy maps (OIM® maps) were acquired. The top plane of specimen H43C1 is *c*(0001), one side plane is *a*(11$\bar{2}$0), and the other one is *m*(10$\bar{1}$0) (Fig. 8).

The OIM® maps display the EBSD pattern quality parameter by grey levels. Bright pixels relate to sharp diffraction patterns indicating intact crystal spots (areas), and dark levels mean high density of near surface defects, boundaries, obstacles like holes or insufficient surface preparation. Black color is assigned to pixels with non-reliable indexing of the acquired EBSD pattern, defined by a threshold in the confidence index $CI < 0.1$. Twin orientations are highlighted by superimposed color in the maps as well in the adjacent pole figures (Fig. 9). OIM® maps of both planes are mounted in a 3D-micrograph (Fig. 8) and shows on side planes (*m*) and (*a*) three sets of *r*-twin lamellae which are coloured in blue, red, and green. The local pole figures of the side plane *m*(10$\bar{1}$0) of the prismatic specimen are calculated from the orientation data and presented in Fig. 9.

Later, the data were analysed with the free and public domain software MTEX. The spatially indexed orientation measurements were RGB- and IHS-colour coded, i.e. a triple of Euler angles was associated with corresponding colours, and plotted in the (*x*, *y*)-plane of measurements (Fig. 10). Neglecting their (*x*, *y*)-position, they

Fig. 11 Pole point plots (equal area projection, upper hemisphere) of the crystal forms $c(0001)$, $r(01\bar{1}2)$, $f(10\bar{1}1)$, $e(10\bar{1}4)$, $a(11\bar{2}0)$, and $m(10\bar{1}0)$
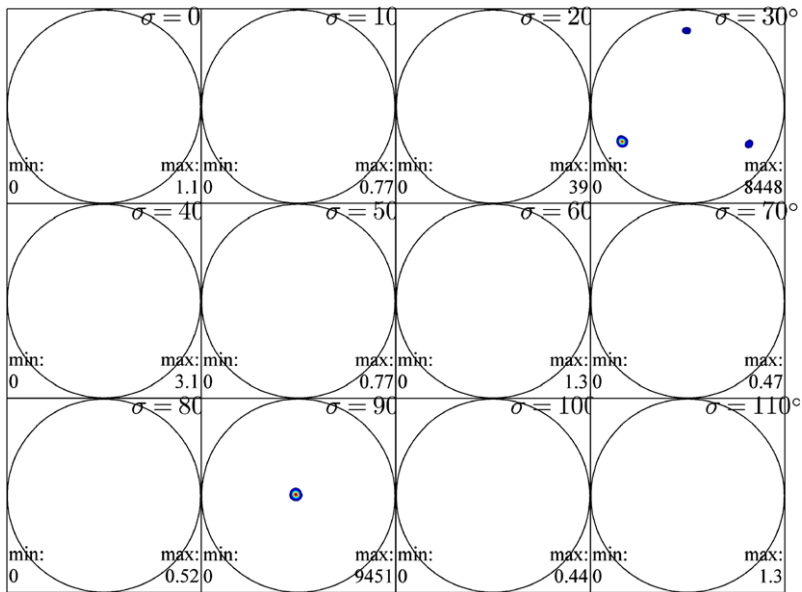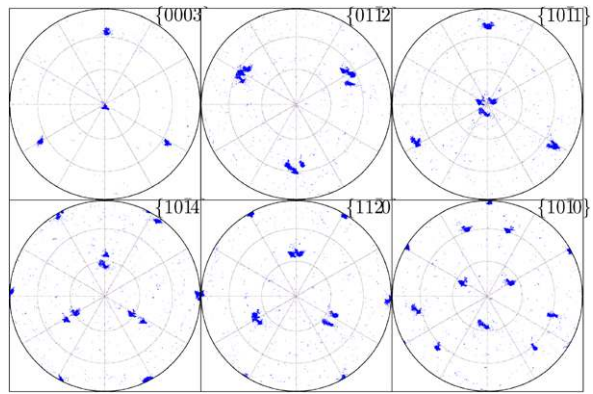

Fig. 12 σ-sections of MTEX's estimated ODF based on EBSD measurements and non-parametric kernel density estimation with the de la Vallée Poussin kernel

were also displayed as scatter plot in Rodrigues space (Fig. 10). Then, corresponding pole point plots were computed and are displayed in Fig. 11.

Non-parametric kernel ODF estimation was done with a de la Vallée Poussin kernel with a halfwidth of 2.0 degrees corresponding to the finite bandwidth of $L = 213$ of the series expansion into generalized spherical harmonics. Its σ-sections are displayed in Fig. 12, the corresponding pole density functions of the crystal forms $c(0001)$, $r(01\bar{1}2)$, $f(10\bar{1}1)$, $e(10\bar{1}4)$, $a(11\bar{2}0)$, and $m(10\bar{1}0)$ augmented with the major mode $(100, 178, 11)$ (black), and minor modes $(90, 65, 59)$ (blue), $(30, 115, 1)$ (red), and $(150, 115, 1)$ (green) are depicted in Fig. 13. Even though the major mode $(155, 3, 53)$ of Neutron diffraction data and the major mode $(100, 178, 11)$ of elec-

Fig. 13 Corresponding computed pole density functions of the crystal forms $c(0001)$, $r(01\bar{1}2)$, $f(10\bar{1}1)$, $e(10\bar{1}4)$, $a(11\bar{2}0)$, and $m(10\bar{1}0)$ augmented with major mode $(100, 178, 11)$ (*black*), and minor modes $(90, 65, 59)$ (*blue*), $(30, 115, 1)$ (*red*), and $(150, 115, 1)$ (*green*), respectively
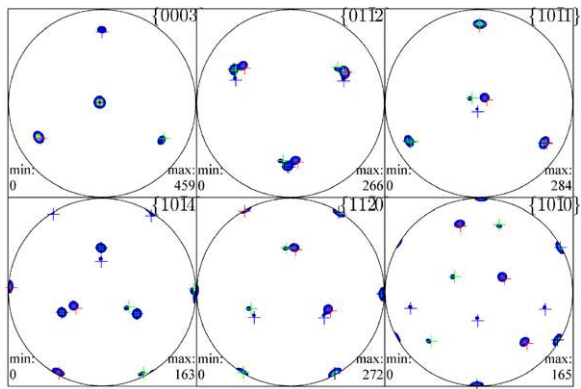

Fig. 14 Pole point plots (equal area projection, upper hemisphere) of the crystal forms $c(0001)$, $f(10\bar{1}1)$, $r(01\bar{1}2)$, $e(10\bar{1}4)$, $a(11\bar{2}0)$, and $m(10\bar{1}0)$ colour coded according to their classification with respect to modes of the estimated ODF, and augmented with major mode $(100, 178, 11)$ (*black*), and minor modes $(90, 65, 59)$ (*blue*), $(30, 115, 1)$ (*red*), and $(150, 115, 1)$ (*green*), respectively, computed and displayed with MTEX
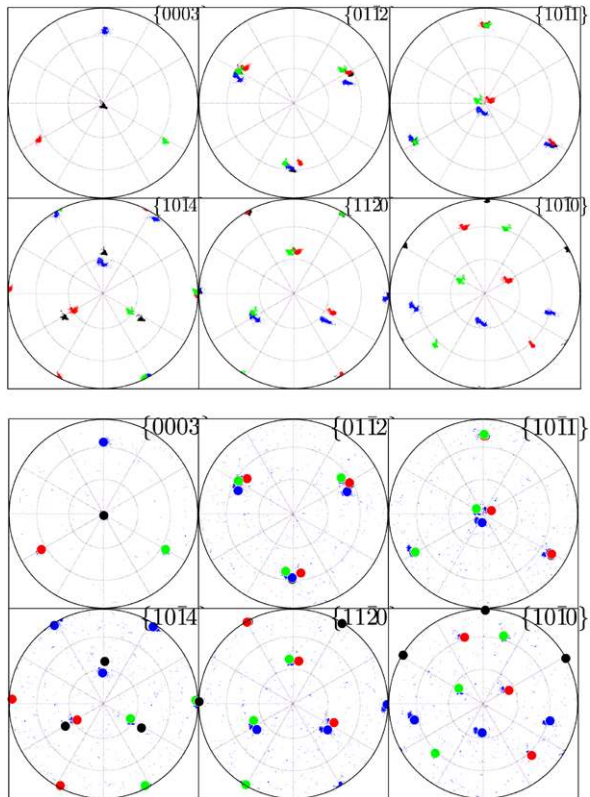

tron back scatter diffraction data look different, they are not. A crystallographically symmetrical equivalent orientation of $(100, 178, 11)$ is $(-80, 2, -71)$. Considering that for small angles β the orientation is approximately given by $\alpha + \gamma$, this sum is $155 + 53 = 208$ degrees for the Neutron diffraction data and $-80 - 71 + 360 = 209$ degrees for the electron back scatter diffraction data. In fact, the difference of the two modal orientations considering crystal symmetry is smaller than 5 degrees, which is

Table 2 The major mode g_M and the three minor modes g_{m_i}, $i = 1, 2, 3$, are given in terms of Euler angles (α, β, γ) (zyz-convention) (left column), and characterized by their probability mass according to the orientation density function in a ball $b(g_m; 10)$ of 10 degrees (center column), and their values of the orientation density function $f(g_m)$

EBSD	(α, β, γ)	$\int_{b(g_m;10)} f(g)\,dg$	$f(\alpha, \beta, \gamma)$
g_M (black)	(100, 178, 11)	0.45	12, 251
g_{m_1} (blue)	(90, 65, 59)	0.05	699
g_{m_2} (red)	(30, 115, 1)	0.04	450
g_{m_3} (green)	(150, 115, 1)	0.33	2, 611
Sum		0.42	

Fig. 15 EBSD measurements of specimen H43C1 colour coded according to their classification with respect to modes of the estimated ODF
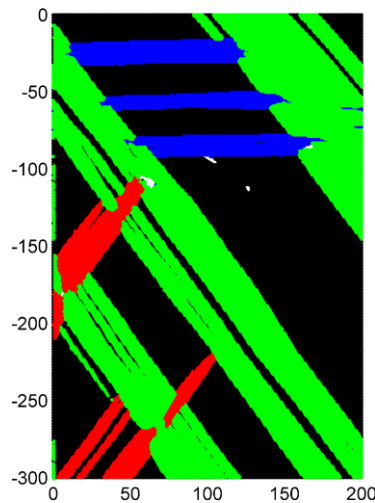
interpreted as being in fair agreement. Then, the EBSD measurements were classified according to 10 degree neighbourhoods of the major and the three minor modes, respectively, and the classes were colour coded with the same colours as the modes themselves. Figure 14 shows the corresponding classified pole point plots, Fig. 15 shows the corresponding spatial map of classified EBSD measurements. A numerical summary of texture estimated from individual orientation measurements includes a texture index $J = 3400$, an entropy $E = -7.42$, and modes as compiled in Table 2.

7 Conclusions

Focusing on the methodological aspects we are lead to the brief conclusion that the results of texture analyses based on integral Neutron diffraction data and on individual electron back scatter diffraction data agree very well.

It is once more confirmed that an interpretation of an orientation probability density function in terns of its individual values may be deceiving. As for any density

function, a proper interpretation is accomplished in terms of volume portions only. Thus, MTEX features a unique approach to analyse individual or integral orientation measurements.

References

Bunge H-J (1969) Mathematische Methoden der Texturanalyse. Akademie Verlag, Berlin

Bunge H-J, Morris PR (1982) Texture analysis in materials science—mathematical methods. Butterworth, Stoneham

Dunkl CF (1966) Operators and harmonic analysis on the sphere. Trans Am Math Soc 125:250–263

Freeden W, Gervens T, Schreiner M (1998) Constructive approximation on the sphere. Clarendon, Oxford

Hall P, Watson GS, Cabrera J (1987) Kernel density estimation with spherical data. Biometrika 74:751–762

Hielscher R (2007) The radon transform on the rotation group—inversion and application to texture analysis. PhD thesis, TU Bergakademie Freiberg, Germany

Hielscher R, Schaeben H (2008a) A novel pole figure inversion method: specification of the MTEX algorithm. J Appl Crystologr 41:1024–1037

Hielscher R, Schaeben H (2008b) Multi-scale texture modeling. Math Geosci 40:63–82

Jansen E, Schäfer W, Kirfel A (2000) The Jülich neutron diffractometer and data processing in rock texture investigations. J Struct Geol 22:1559–1564

Kunze K, Wright SI, Adams BL, Dingley DJ (1993) Advances in automatic EBSD single orientation measurements. Textures Microstruct 20:41–54

Matthies S, Vinel GW, Helming K (1987) Standard distributions in texture analysis, vol 1. Akademie Verlag, Berlin

Morawiec A (1997) Distributions of misorientation angles and misorientation axes for crystallites with different symmetries. Acta Crystologr A 53:273–285

Parzen E (1962) On estimation of a probability density function and mode. Ann Math Stat 33:1065–1076

Paterson MS (1970) A high pressure, high-temperature apparatus for rock deformation. Int J Rock Mech Min Sci 7:517–526

Paterson MS (1990) Rock deformation experimentation. In: Duba AG, Durham WB, Handin JW, Wang HF (eds) The brittle-ductile transition in rocks; the heard volume. American geophysical union geophysical monograph, vol 56, pp 187–194

Schaeben H (1982) Fabric-diagram contour precision and size of counting element related to sample size by approximation theory methods. Math Geol 14:205–216. Erratum: Math Geol 15:579–580

Schaeben H (1997) A simple standard orientation density function: the hyperspherical de la Vallée Poussin kernel. Phys Stat Sol B 200:367–376

Schaeben H (1999) The de la Vallée Poussin standard orientation density function. In: Proceedings of the international conference on neutron texture and stress analysis, Dubna, Russia, 23–26 June 1997. Special Issue Textures Microstruct 33:365–373

Schaeben H, Boogaart KGvd (2003) Spherical harmonics in texture analysis. Tectonophysics 370:253–268

Schaeben H, Hielscher R, Fundenberger J-J, Potts D, Prestin J (2007) Orientation density function-controlled pole probability density function measurements: automated adaptive control of texture goniometers. J Appl Cryst 40:570–579

Scott DW (1992) Multivariate density estimation—theory, practice, and visualization. Wiley, New York

Siemes H, Klingenberg B, Rybacki E, Naumann M, Schäfer W, Jansen E, Kunze K (2008) Glide systems of hematite single crystals in deformation experiments. Ore Geol Rev 33:255–279

Tapia RA, Thompson JR (1978) Nonparametric probability density estimation. Johns Hopkins Press, Baltimore